Supporting Information

Bifunctional PdMoPt Trimetallene Boosts Alcohol-water Electrolysis

Junfeng Liu*[a], Tong Li,[a] Qiuxia Wang,[a] Haiting Liu,[a] Jingjing Wu,[b, c] Yanping Sui,[b] Huaming Li,[a] Pengyi Tang,*[b,c,d] Yong Wang*[a]

[a] Institute for Energy Research, School of Chemistry and Chemical Engineering, Jiangsu University, Zhenjiang 212013, China

[b] National Key Laboratory of Materials for Integrated Circuits, Shanghai Institute of Microsystem and Information Technology (SIMIT), Chinese Academy of Sciences (CAS), Shanghai, 200050 China

[c] 2020 X-Lab, ShangHai Institute of Microsystem and Information Technology, Chinese Academy of Sciences, Shanghai 200050, China

[d] School of Graduate Study, University of Chinese Academy of Sciences, Beijing 100049, China

[*] Corresponding authors

Email addresses: jliu@ujs.edu.cn (J. Liu); py.tang@mail.sim.ac.cn (P. Tang); wangyong@ujs.edu.cn (Y. Wang)

Experimental Section

Chemicals and materials

Palladium(II) acetylacetonate ($Pd(acac)_2$, 98%) and Nafion (10 wt% in water) were obtained from Sigma-Aldrich. $Mo(CO)_6$ (98%) was obtained from Energy Chemical Co. Ltd. Platinum(II) acetylacetonate ($Pt(acac)_2$), 98%) and commercial Pd/C (10% Pd) were purchased from Bide Pharmatech Ltd. A commercial Pt on carbon catalyst (Pt/C, 20% Pt) was purchased from Alfa Aesar. Oleylamine (OAm, approximate C18 content 80-90%) and ascorbic acid (AA, 99.99%) were purchased from Macklin. Potassium hydroxide, chloroform, methanol ethylene glycol, glycerol and isopropanol were of analytical grade and purchased from Sinopharm Chemical Reagent Co. Ltd. All reagents were used as received without further purification.

Synthesis of PdMoPt trimetallene

In a typical synthesis, a mixture was prepared by adding 20 mg of $Pd(acac)_2$, 10 mg of $Mo(CO)_6$, 60 mg of ascorbic acid and 10mL of oleylamine into a 30 mL glass vial. The vial was then sealed and subjected to sonication for 1 h to obtain a homogeneous solution. The resulting solution was heated to 60 ℃ while maintaining continuous magnetic stirring for 12 h. Subsequently, 10 mg of $Pt(acac)_2$ was introduced into the vial, and the reaction temperature was further increased to 165 ℃ and held for 1 h. Afterward, the mixture was allowed to cool down to ambient temperature naturally. The resulting black product was transferred into centrifuge tubes, followed by centrifugation at 8000 rpm for 5 min to separate the catalyst from the reaction mixture. The purification process was achieved by twice performing dispersion/precipitation steps using chloroform and ethanol. For comparison, PdMoPt trimetallene with a lower amount of Pt was produced using the same procedure, except the reaction temperature in the second step was set to 150 ℃ for 1 h. Additionally, PdMoPt trimetallene was synthesized by a one-pot procedure using the same amounts of $Pd(acac)_2$, $Mo(CO)_6$, ascorbic acid, oleylamine, and $Pt(acac)_2$ in the glass vial, and reacting at 165 ℃ for 1 h.

Synthesis of PdMo bimetallene

In a typical synthesis, a mixture was prepared by adding 20 mg of $Pd(acac)_2$, 10 mg of $Mo(CO)_6$, 60 mg of ascorbic acid and 10mL of oleylamine into a 30 mL glass vial. The vial was then sealed and subjected to sonication for 1 h to obtain a homogeneous solution. The resulting solution was heated to 60 ℃ while maintaining continuous magnetic stirring for 12 h. Afterward, the mixture was allowed to cool down to ambient temperature naturally. The resulting black product was transferred into centrifuge tubes, followed by centrifugation at 8000 rpm for 5 min to separate the catalyst from the reaction mixture. The purification process was achieved by twice performing dispersion/precipitation steps using chloroform and ethanol. For comparison, PdMo bimetallene was also produced using 5 mg and 20 mg of $Mo(CO)_6$ in the synthesis, while keeping all other reaction conditions the same.

Synthesis of PdPt bimetallene

In a typical synthesis, a mixture was prepared by adding 20 mg of $Pd(acac)_2$, 60 mg of ascorbic acid and 10mL of oleylamine into a 30 mL glass vial. The vial was then sealed and subjected to sonication for 1 h to obtain a homogeneous solution. The resulting solution was heated to 60 ℃ with bubbling CO gas for 10 min. Subsequently, 10 mg of $Pt(acac)_2$ was introduced into the vial, and the reaction temperature was further increased to 165 ℃ and held for 1 h. Afterward, the mixture was allowed to cool down to ambient temperature naturally. The resulting black product was transferred into centrifuge tubes, followed by centrifugation at 8000 rpm for 5 min to separate the catalyst from the reaction mixture. The purification process was achieved by twice performing dispersion/precipitation steps using chloroform and ethanol.

Preparation of catalysts

10 mL of an aqueous 0.05 M hydrazine hydrate was introduced into the vial containing as-produced nanomaterials in 10 ml of toluene. The mixture underwent stirring at room temperature for more than 1 h. The product was subjected to repetitive purification cycles involving the use of chloroform, deionized water, and ethanol. The final product was obtained through the drying of the resulting precipitate under ambient conditions.

To prepare the catalyst ink for electrochemical measurements, a homogeneous slurry was formed by combining 1 mg of PdMoPt trimetallene, 2 mg of carbon black, 20 μL of a 10% Nafion solution, 0.25 mL of isopropanol, and 0.75 mL of deionized water, followed by sonication for 1 h. For comparison, a PdMo and PdPt ink were also prepared by mixing 1 mg of PdMo or PdPt bimetallene, 2 mg of carbon black, 20 μL of 10% Nafion, 0.25 mL isopropanol, and 0.75 mL of deionized water in accordance with the same procedural steps. Furthermore, commercial Pt/C and Pd/C inks were also prepared using identical procedures, entailing the combination of 3 mg of Pt/C or Pd/C with equivalent quantities of Nafion solution, isopropanol, and deionized water.

Characterization

X-ray diffraction (XRD) was performed on the sample supported on a silica glass substrate using a Bruker-AXS D8 X-ray diffractometer with Cu Kα radiation (λ = 1.5418 Å) operating at 40 kV and 40 mA. Transmission electron microscopy (TEM) characterization was carried out using a ZEISS LIBRA 120, operating at 120 kV and a JEOL 1011 operating at 100 kV. Carbon-coated TEM grids from Electron Microscopy China were used as substrates. High-resolution TEM (HRTEM) studies were conducted using a field emission gun FEI™ Tecnai G2 F30 microscope at 200 kV. High angle annular dark-field scanning transmission electron microscope (HAADF-STEM) was performed on the JEM-ARM300F at 300 kV. Inductively coupled plasma optical emission spectrometry (ICP-OES) analyses were conducted using an Agilent 720ES instrument. X-ray photoelectron spectroscopy (XPS) was analyzed on a Thermo Scientific K-Alpha XPS system equipped with an Al Kα source (hv = 1486.6 eV) operating at 12 kV and 6 mA, and binding energy values were referred to the adventitious C 1 s peak at 284.8 eV.

Electrochemical measurements

Electrochemical measurements were conducted on a CHI660E electrochemical workstation (CH Instruments Inc., Shanghai) at room temperature with a standard three-electrode system. A Hg/HgO (1 M KOH) electrode was used as the reference electrode, and a platinum mesh was used as the counter electrode. The working electrode was

prepared by drop-casting 3.0 μL of the catalyst ink on a glassy carbon electrode (GCE, 3 mm in diameter) and drying it naturally at room temperature. The cyclic voltammetry (CV) curves were recorded from -0.924 to 0.4 V versus Hg/HgO at a scan rate of 50 mV s^{-1} in N_2-saturated 1.0 M KOH solution. The methanol oxidation reaction (MOR), ethylene glycol oxidation reaction (EGOR), and glycerol oxidation reaction (GOR) polarization curves were obtained at the scan rate of 50 mV s^{-1} in 1 M KOH + 1 M CH_3OH solution, 1 M KOH + 1 M $(CH_2OH)_2$ solution, and 1 M KOH + 1 M $C_3H_5(OH)_3$ solution, respectively. Electrochemical impedance spectra (EIS) were conducted at a bias of -0.3 V vs. Hg/HgO in the frequency range from 100 kHz to 0.1 Hz with an amplitude of 5 mV. The chronoamperometry (CA) measurements of MOR, EGOR, and GOR were conducted in the corresponding electrolyte at -0.1 V, -0.1 V and -0.05 V versus Hg/HgO, respectively. For HER measurements, polarization curves were tested from -0.9 V to -1.5 V versus Hg/HgO in a 1 M KOH solution. Linear sweep voltammetry (LSV) was obtained at a scan rate of 5 mV s^{-1}. Cycling stability tests were performed in 1 M KOH at 100 mV s^{-1} for 1000 and 3000 cycles. The chronopotentiometry test was recorded at 10 and 100 mA cm^{-2} for 12 h. The turnover frequency (TOF) was determined according to the equation:

$$TOF = \frac{\mathrm{J} \times \mathrm{A}}{\mathrm{z} \times \mathrm{F} \times \mathrm{n}}$$

Where J (A cm^{-2}) is the current density measured at a specific potential, A (cm^2) is the geometric surface area of the working electrode, z is the electron transfer number per molecule generated, n is the number of moles of the catalysts on the electrode, and F is Faraday constant. Normalizing by mass or surface active sites of catalysts gives TOF_{mass} and $TOF_{surface}$, respectively.

Computational details

All calculations were performed using the Vienna ab initio simulation package (VASP) code.[1,2] The Perdew–Burke–Ernzerhof functional with a generalized gradient approximation was employed to describe the electronic exchange-correlation energy.[3,4] The projector augmented-wave method was applied, and an energy cutoff of 400 eV was utilized.[5] Sampling over the Brillouin zone was performed using the Monkhorst-

Pack type, employing a 3 × 3 × 1 k-point mesh. Long-range van der Waals (vdW) interactions were accounted for using the DFT-D3 method with Becke-Johnson damping.[6,7] Geometry optimization was considered converged when the maximal residual energy and force were below 10^{-5} eV and -0.03 eV·Å^{-1}, respectively. To avoid pseudo interactions between periodic units, a vacuum slab of 15 Å was introduced in the z-direction. Thermodynamic free energies were defined as $G = E_{DFT} + E_{ZPE} - TS$, Where E_{DFT}, E_{ZPE}, and TS represent the DFT total energy, zero-point energy (ZPE), and entropy, respectively.

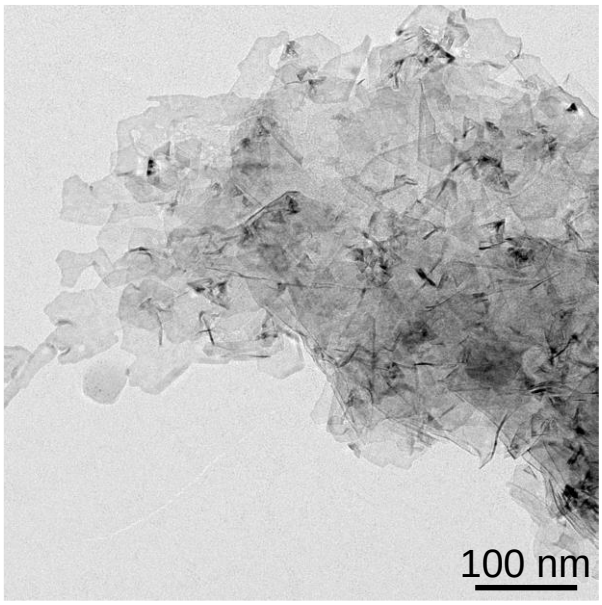

Fig. S1. TEM image of PdMo bimetallene.

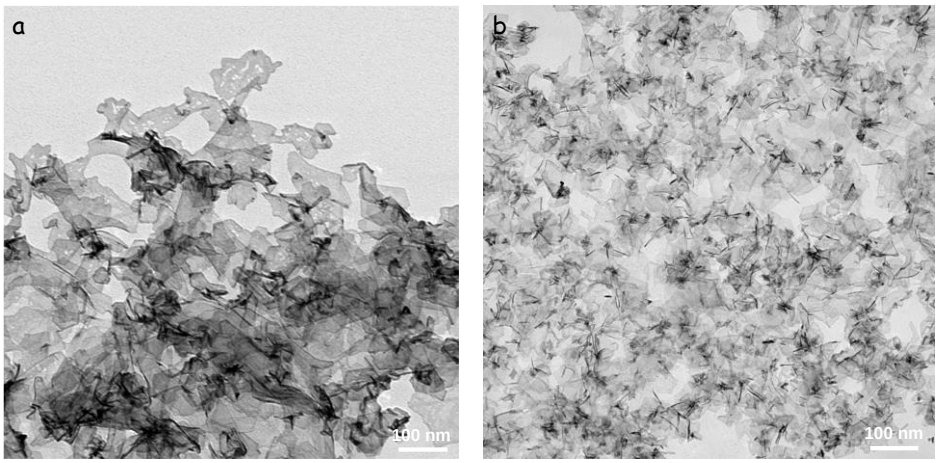

Fig. S2. TEM images of PdMo bimetallene synthesized using (a) 5 mg and (b) 20 mg of $Mo(CO)_6$.

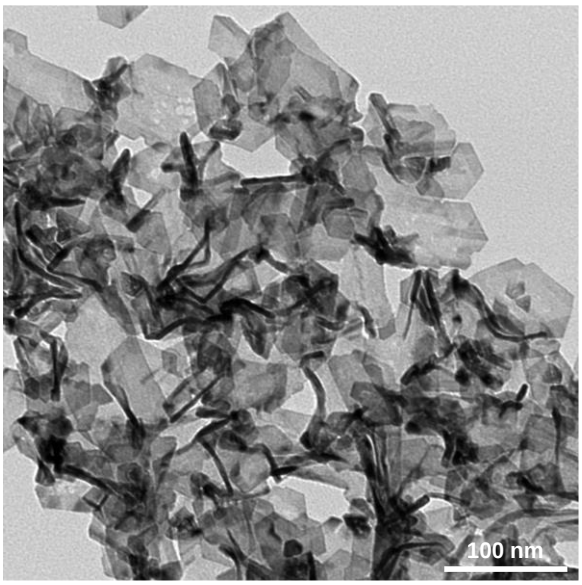

Fig. S3. TEM image of PdMoPt trimetallene synthesized by the one-pot procedure.

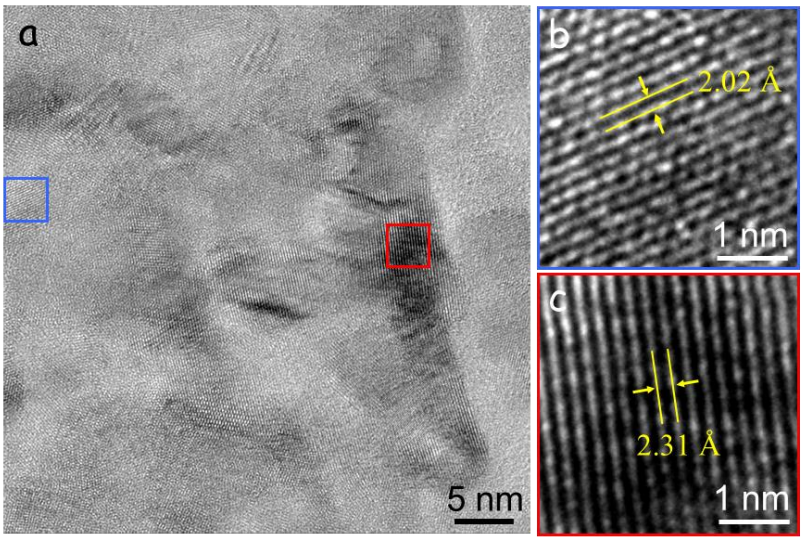

Fig. S4. Representative HRTEM images of a PdMo bimetallene sheet, and (b) its magnified view of the blue square area and (c) the magnified view of the red square area.

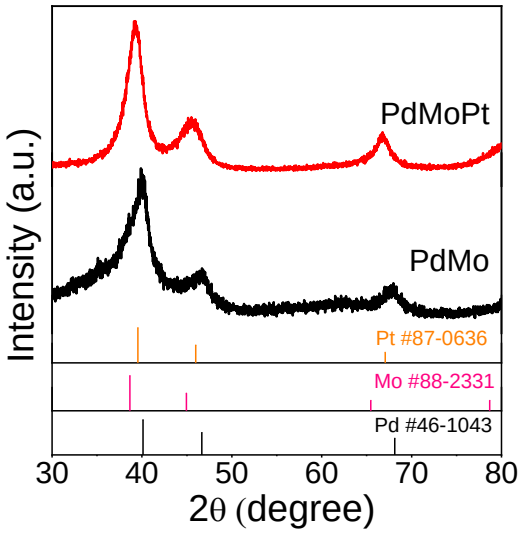

Fig. S5. XRD patterns of PdMo bimetallene and PdMoPt trimetallene.

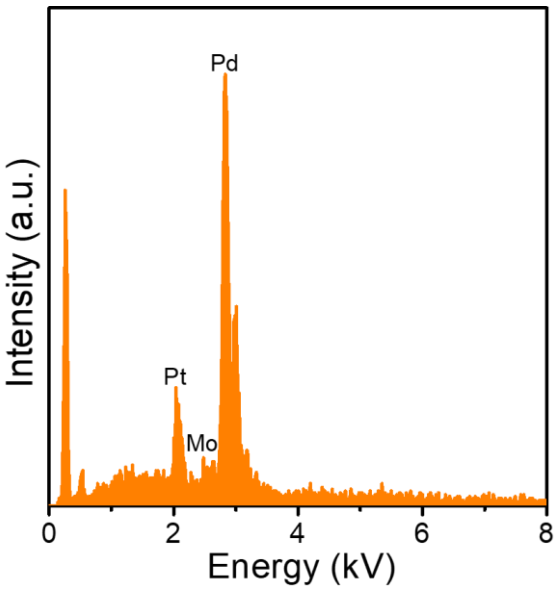

Fig. S6. EDX elemental composition of the PdMoPt trimetallene.

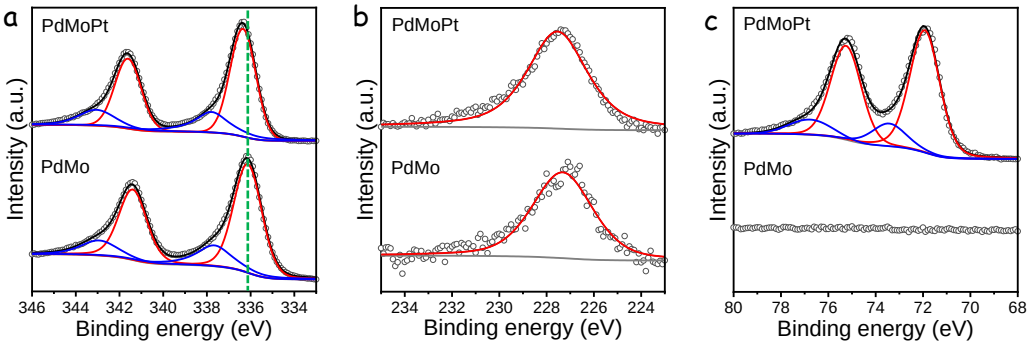

Fig. S7. XPS spectra in the (a) Pd 3d, (b) Mo 3d and (c) Pt 4f regions for PdMoPt trimetallene and PdMo bimetallene.

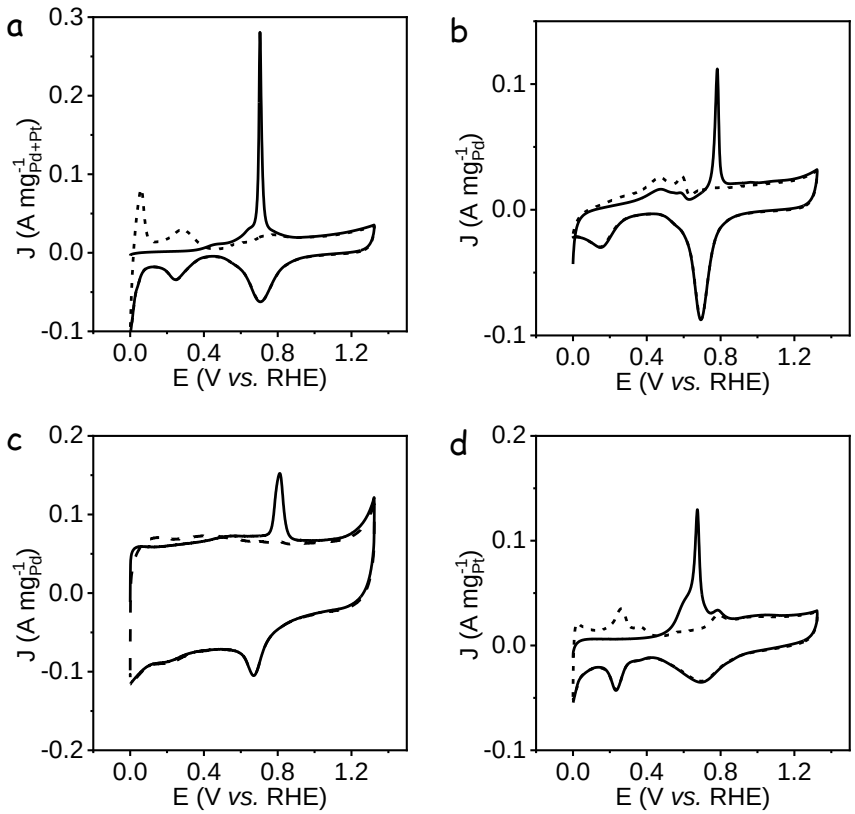

Fig. S8. CO stripping voltammetry of (a) PdMoPt, (b) PdMo, (c) Pd/C and (d) Pt/C in 1 M KOH solution. The solid line shows the first scanning cycle, and the dashed line shows the second scanning cycle.

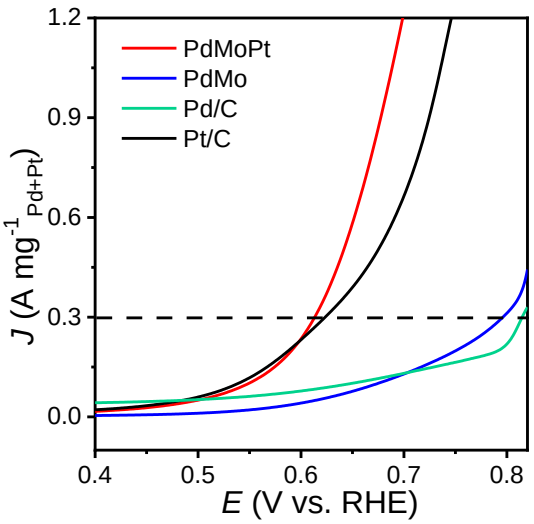

Fig. S9. The onset potential calculated at 0.3 A mg^{-1}_{Pd+Pt} of catalysts in the forward scan toward MOR.

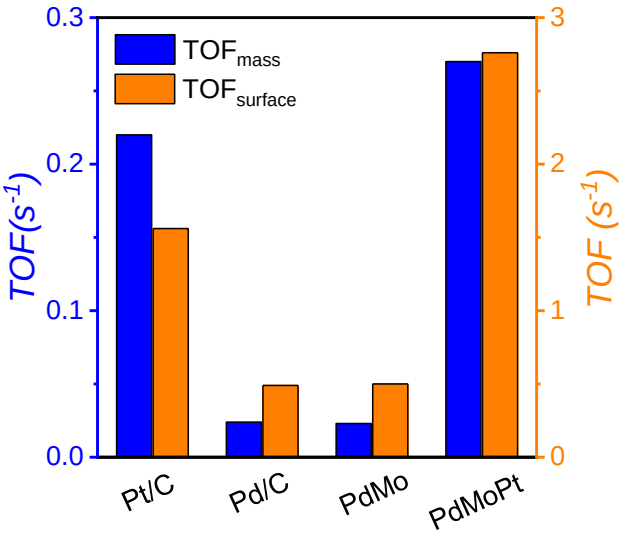

Fig. S10. Comparison of TOF_{mass} and $TOF_{surface}$ of the catalysts for MOR.

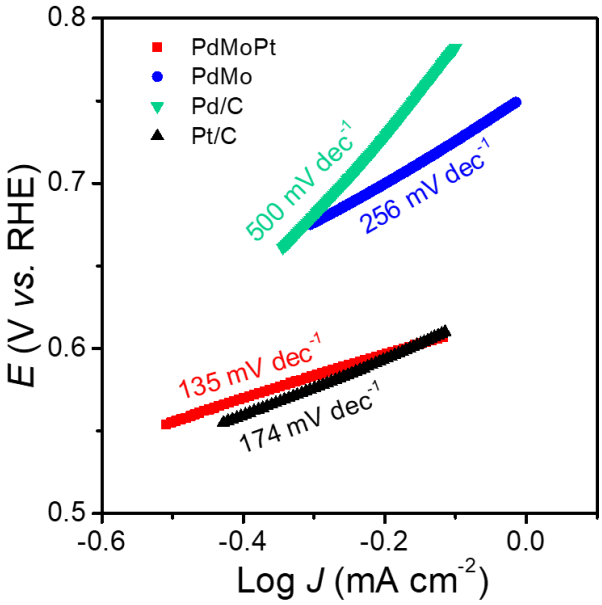

Fig. S11. Tafel plots of the catalysts calculated from CV curves in the potential range between 0.5 and 0.8 V.

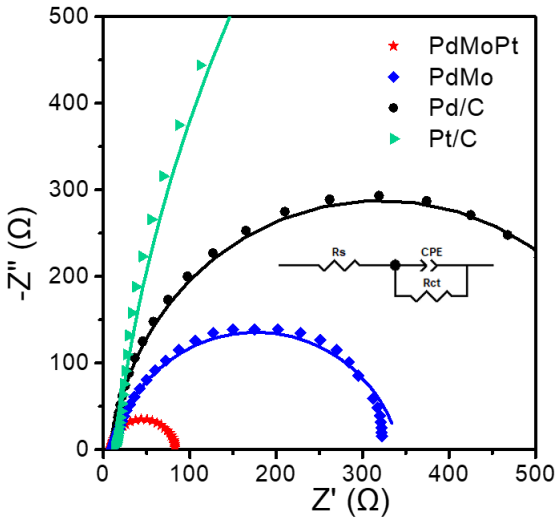

Fig. S12. Nyquist plots of the catalysts measured at -0.3 V vs. Hg/HgO in 1 M KOH with 1 M methanol solution.

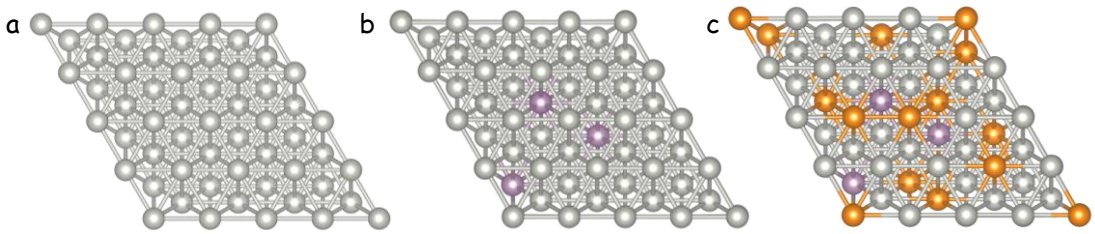

Fig. S13. Crystal structure models of (a) Pd, (b) PdMo and (c) PdMoPt.

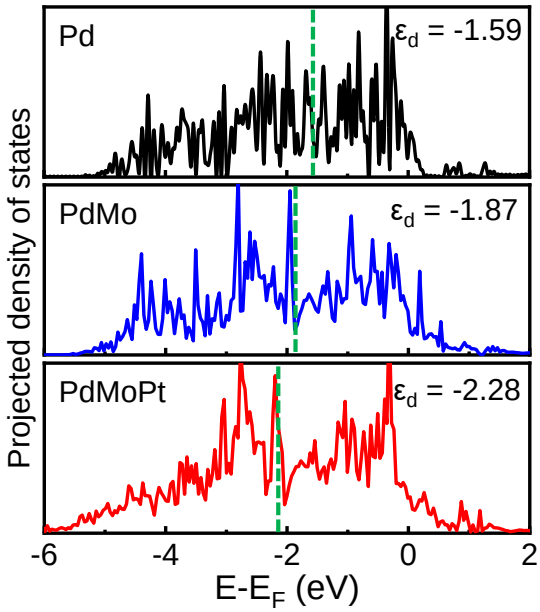

Fig. S14. PDOS of the d-band for the surface Pd atoms in Pd, PdMo and PdMoPt. The horizontal dashed lines indicate the calculated d-band center.

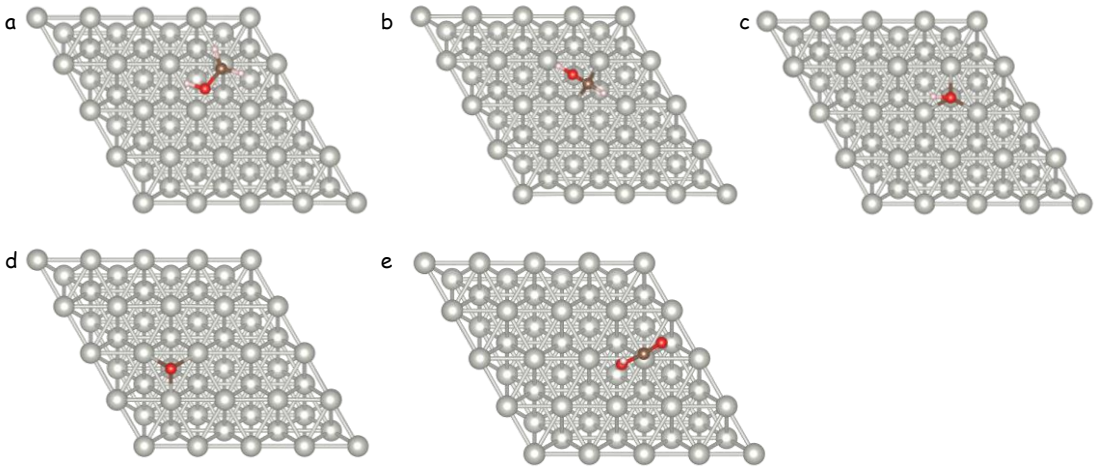

Fig. S15. Crystal structure models of (a) CH_2OH*, (b) CHOH*, (c) COH*, (d) CO* and (e) COOH* on Pd (111) surface.

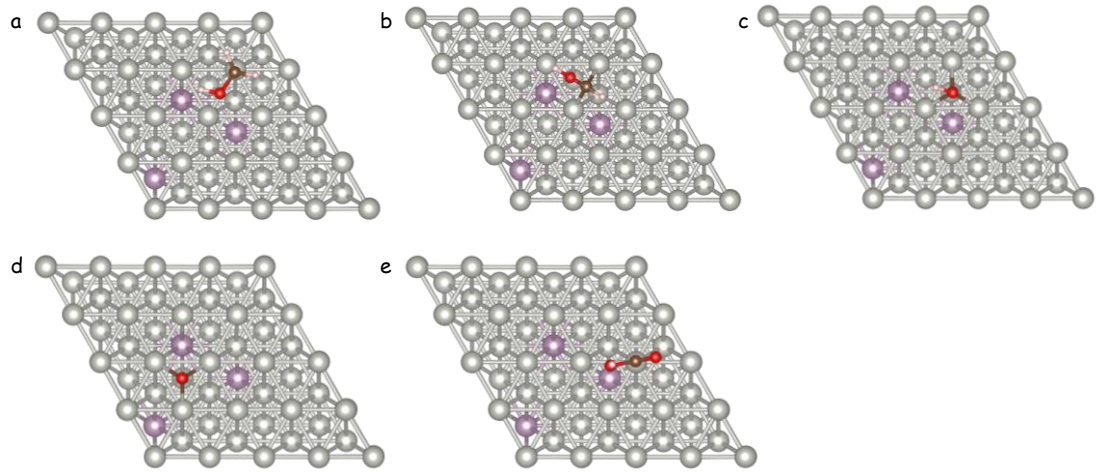

Fig. S16. Crystal structure models of (a) CH_2OH*, (b) CHOH*, (c) COH*, (d) CO* and (e) COOH* on PdMo (111) surface.

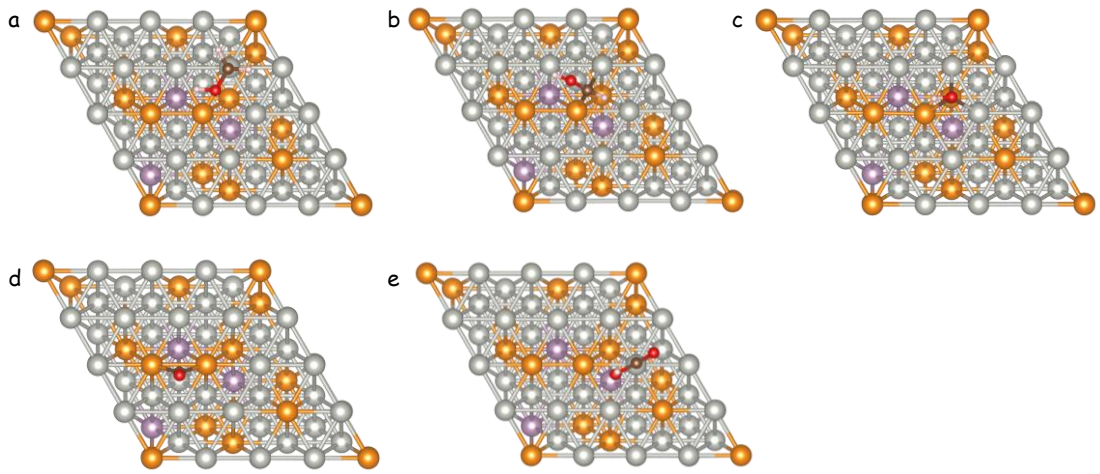

Fig. S17. Crystal structure models of (a) CH_2OH*, (b) CHOH*, (c) COH*, (d) CO* and (e) COOH* on PdMoPt (111) surface.

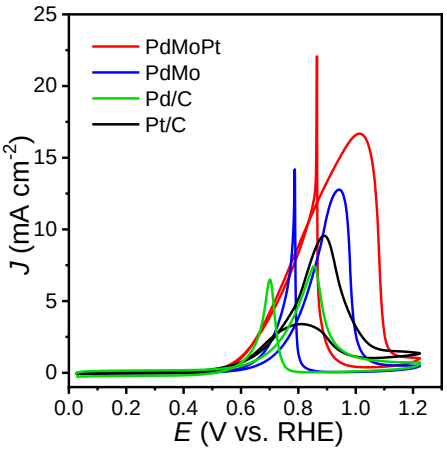

Fig. S18. CV curve of catalysts toward EGOR in a 1 M KOH with 1 M ethylene glycol solution.

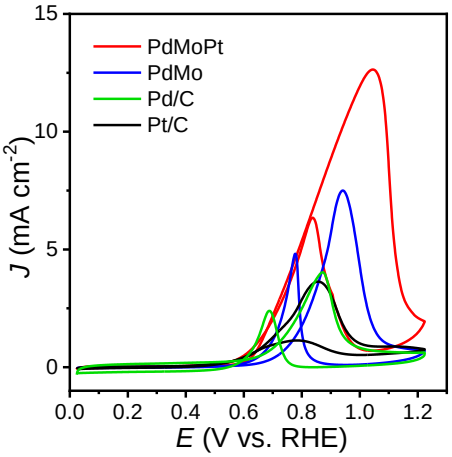

Fig. S19. CV curve of catalysts toward GOR in a 1 M KOH with 1 M glycerol solution.

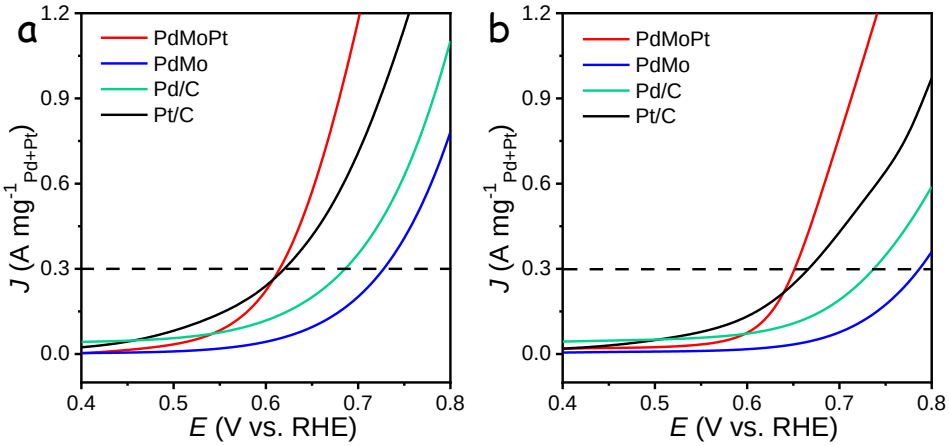

Fig. S20. The onset potential calculated at 0.3 A mg^{-1}_{Pd+Pt} of catalysts in the forward scan toward (a) EGOR and (b) GOR.

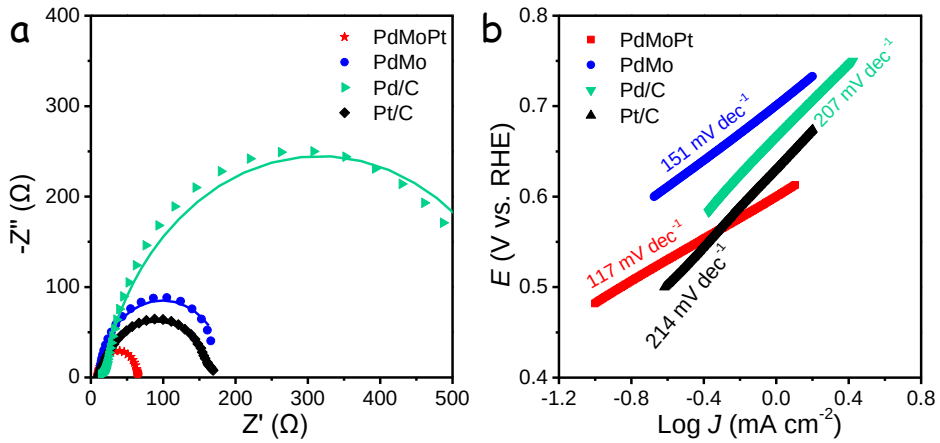

Fig. S21. (a) Nyquist plots of the catalysts measured at -0.3 V vs. Hg/HgO in 1 M KOH with 1 M ethylene glycol solution. (b) Tafel plots of the catalysts calculated from CV curves in the potential range between 0.4 and 0.8 V in 1 M KOH with 1 M ethylene glycol solution.

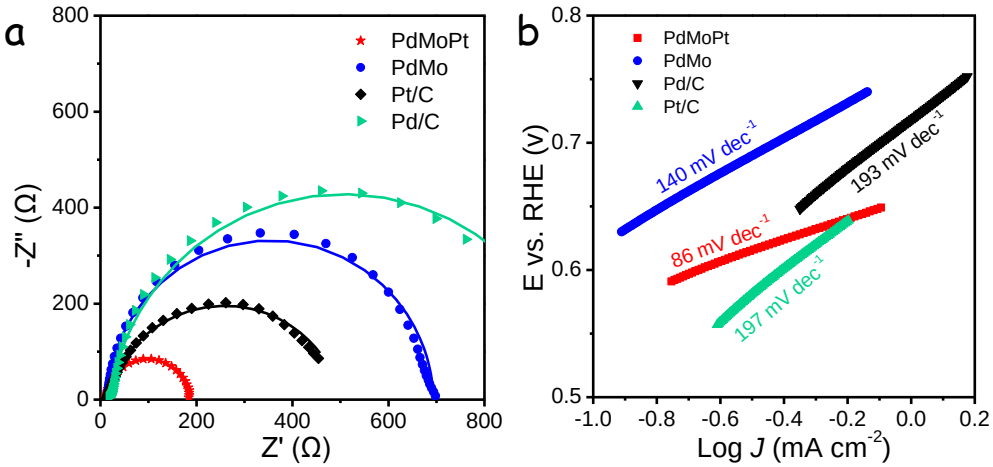

Fig. S22. (a) Nyquist plots of the catalysts measured at -0.3 V vs. Hg/HgO in 1 M KOH with 1 M glycerol solution. (b) Tafel plots of the catalysts calculated from CV curves in the potential range between 0.5 and 0.8 V in 1 M KOH with 1 M glycerol solution.

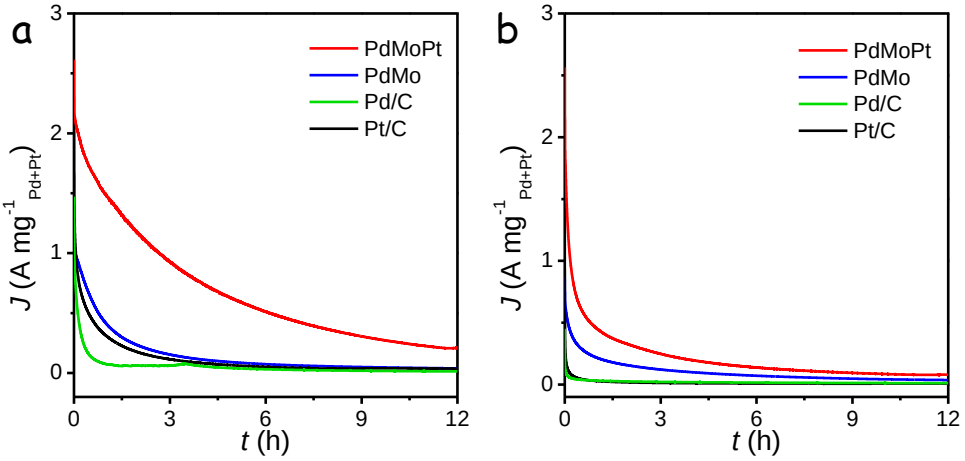

Fig. S23. CA curves of catalysts in (a) 1 M KOH with 1 M ethylene glycol solution and (b) 1 M KOH with 1 M glycerol solution.

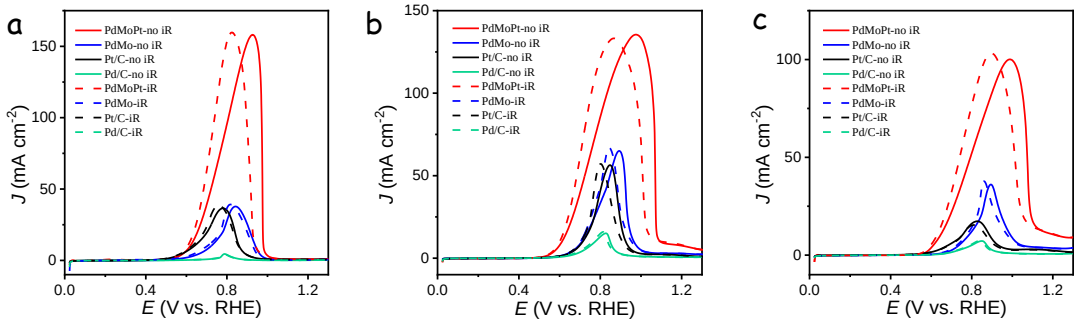

Fig. S24. The comparison of polarization curves normalized to electrode area in (a) 1 M KOH with 1 M methanol solution, (b) 1 M KOH with 1 M ethylene glycol solution and (c) 1 M KOH with 1 M glycerol solution without or corrected with 85% iR compensation.

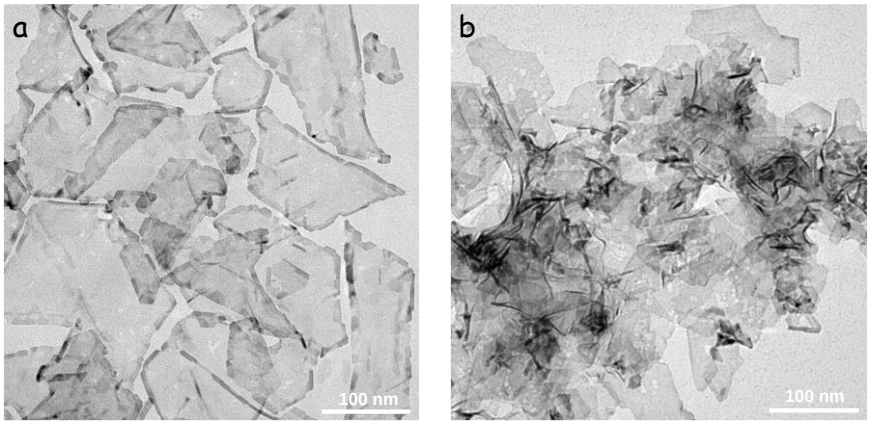

Fig. S25. TEM images of (a) PdPt and (b) PdMoPt with a 7% atomic ratio of Pt.

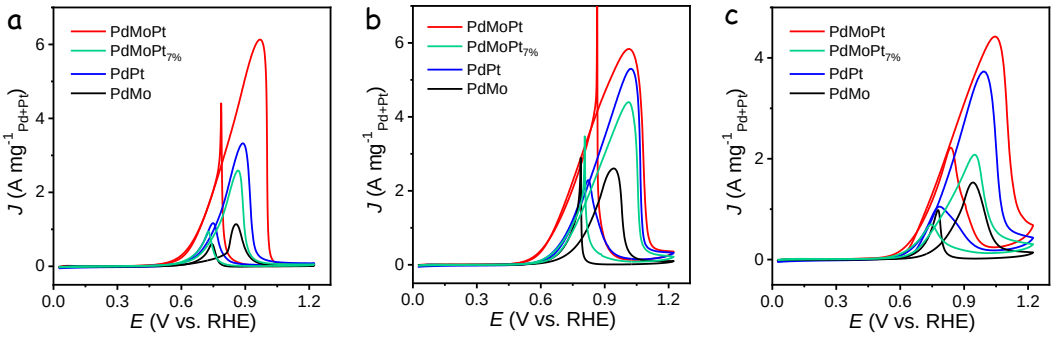

Fig. S26. CV curves of the catalysts toward (a) MOR, (b) EGOR and (c) GOR.

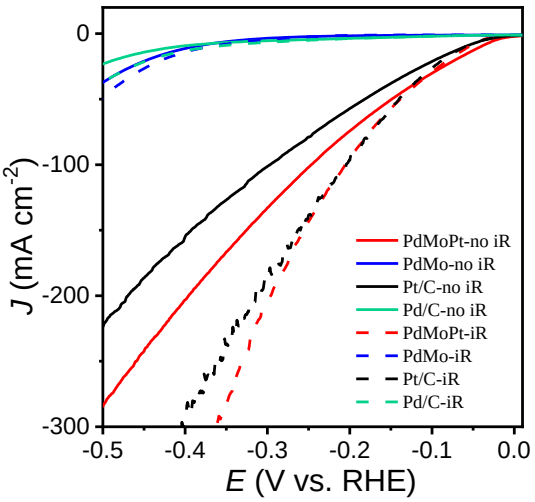

Fig. S27. Comparison of polarization curves of the catalysts for HER without or corrected with 85% iR compensation.

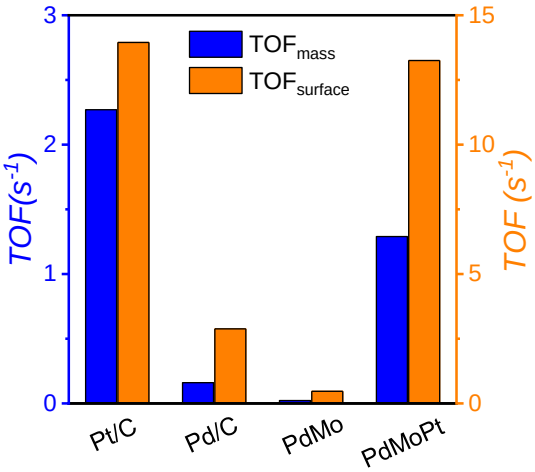

Fig. S28. Comparison of TOF_{mass} and $TOF_{surface}$ of the catalysts for HER.

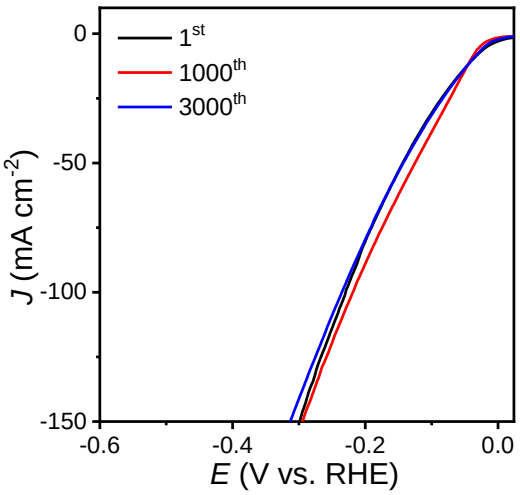

Fig. S29. Polarization curves of PdMoPt catalyst for HER before, after 1000 and 3000 cycles measurement.

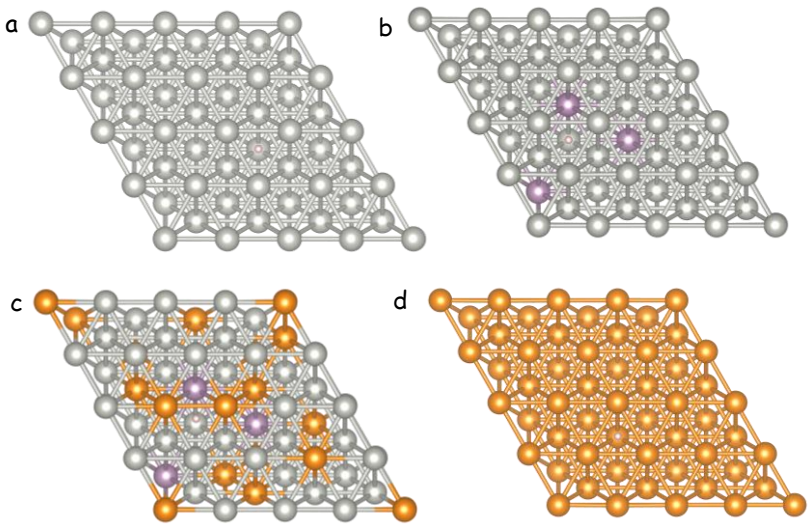

Fig. S30. Structure of H* adsorption on the surface of (a) Pd, (b) PdMo, (c) PdMoPt and (d) Pt surfaces.

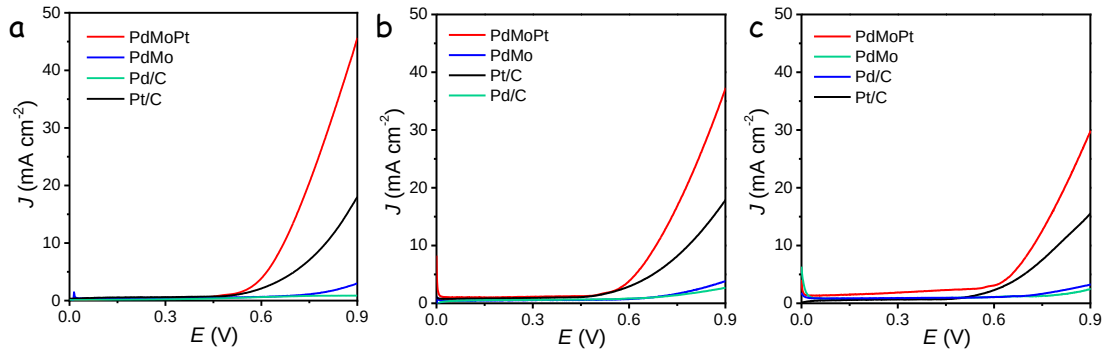

Fig. S31. LSVs of the cells equipped with Pt/C, Pd/C, PdMo and PdMoPt as both anode and cathode catalysts in (a) 1 M KOH with 1 M methanol solution, (b) 1 M KOH with 1 M ethylene glycol solution and (c) 1 M KOH with 1 M glycerol solution.

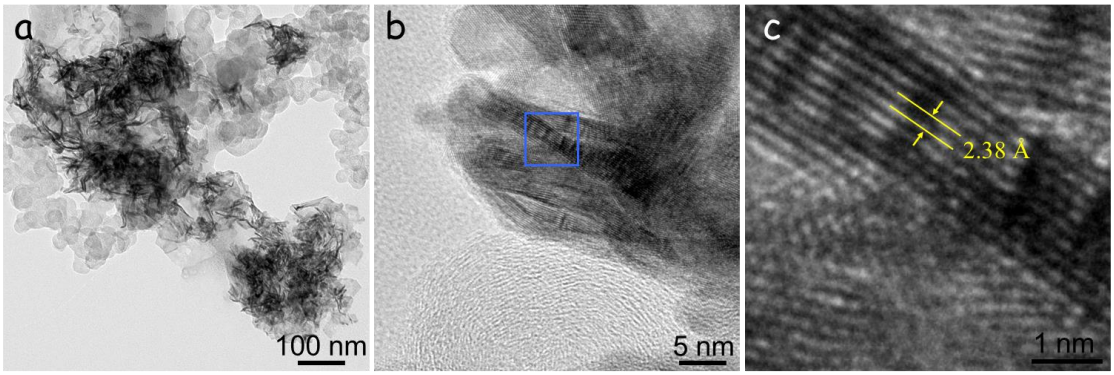

Fig. S32. (a) TEM and (b) HRTEM images of PdMoPt catalyst at anode after the stability measurements and (c) the magnified view of the blue square area in (b) panel.

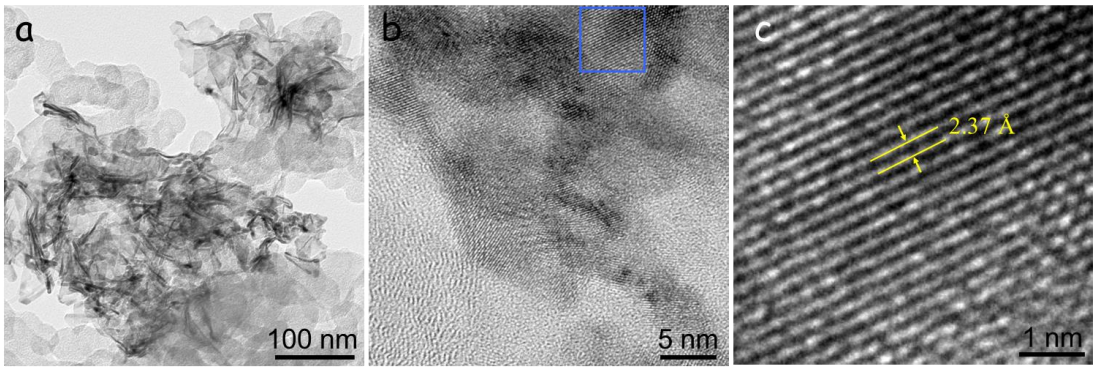

Fig. S33. (a) TEM and (b) HRTEM images of PdMoPt catalyst at cathode after the stability measurements and (c) the magnified view of the blue square area in (b) panel.

Table S1. Comparison of activity and stability of Pt or Pd-based catalysts for MOR.

Catalysts	Electrolyte	J_s (mA cm^{-2})	J_m (A mg^{-1})	Stability (s)	Ref.
PdMoPt	1 M KOH+1 M MeOH	17.52	6.13	43200	This work
Co-N-C/Pt	1 M KOH+3 M MeOH	10.8	5.6	12000	8
PdCu	1 M KOH+1 M MeOH	2.47	1.6	3600	9
Au@Pt-Pd H-Ss	1 M KOH+1 M MeOH	5.04	4.38	-	10
PtNiGaSnMoRe	1 M KOH+1 M MeOH	12.31	6.2	10000	11
CrO_X-Pd	1 M KOH+1 M MeOH	5.3	2.05	5000	12
PdNiCuP	1 M KOH+1 M MeOH	2.49	1.61	-	13
PtBi	1 M KOH+1 M MeOH	11.93	6.42	20000	14
Pd_3Ni_1-TaN/C	1 M KOH+1 M MeOH	2.64	3.64	3600	15
PdRu–RuO_2/C	1 M KOH+1 M MeOH	3.3	1.05	-	16
MoPdH	1 M KOH+1 M MeOH	6.06	3.56	30000	17

Table S2. Comparison of activity and stability of Pt or Pd-based catalysts for EGOR.

Catalysts	Electrolyte	J_s (mA cm^{-2})	J_m (A mg^{-1})	Stability (s)	Ref.
PdMoPt	1 M KOH+1 M EG	15.71	5.50	43200	This work
PdPt	0.5 M KOH+1 M EG	12.6	5.55	3600	18
RhCu	1 M KOH+1 M EG	1.54	0.78	18000	19
Pd_3Ag_1 HNs	1 M KOH+1 M EG	12.8	3.15	3600	20
Ga@PdAgCo/CNT	1 M KOH+1 M EG	3.37	0.30	1000	21
coral-like Pd network	1 M KOH+0.5 M EG	8.81	1.79	7200	22
PdRuCu	0.5 M KOH+0.5 M EG	4.19	1.29	4000	23
$Pt_{0.8}Ru_{0.2}$	0.25 M KOH+0.25 M EG	11.5	6.1	2400	24
Pd/SDMC	1 M KOH +1 M EG	5.26	4	-	25
Pt_4Rh-S	1 M KOH+1 M EG	11.6	5.13	3600	26
fcc-2H-fcc Au@Pd	0.5 M KOH + 0.5 M EG	10.9	5.4	3600	27

Table S3. Comparison of activity and stability of Pt or Pd-based catalysts for GOR.

Catalysts	Electrolyte	J_s (mA cm^{-2})	J_m (A mg^{-1})	Stability (s)	Ref.
PdMoPt	1 M KOH+1 M glycerol	12.49	4.37	43200	This work
PdFe/rGO	1 M KOH+0.1 M glycerol	2.3	1.11	1800	28
PdBi	1 M KOH +1 M glycerol	7.9	3.04	4000	29
Pt-Co	1 M KOH+0.1M glycerol	3.53	1.2	5000	30
Pt_3Ni	1 M KOH +1 M glycerol	7.3	4.25	-	31
PdPtAg	1 M KOH+1 M glycerol	10.65	3.06	3600	32
Pt_3Co_1	1 M KOH+1 M glycerol	7.2	3.75	10800	30
$Pd_{62}Ag_{38}$	1 M KOH+1 M glycerol	6.6	4.14	4000	33
PdRuCu	1 M KOH+0.5 M glycerol	3.88	1.08	6000	34
Pt_3Ni	1 M KOH+1 M glycerol	11.4	4.6	3600	35
Ru-PdRu	1 M KOH+1 M glycerol	9.4	5.84	4000	36

Table S4. The measured solution resistance of catalysts for MOR, EGOR, GOR and HER.

Resistance / Catalysts	R_{MOR}	R_{EGOR}	R_{GOR}	R_{HER}
PdMoPt	9.97	11.56	13.30	9.90
PdMo	9.54	11.51	13.77	10.74
Pt/C	9.96	12.35	13.76	10.59
Pd/C	10.72	12.35	14.47	9.90

References

1 G. Kresse and J. Hafner, *Phys. Rev. B*, 1993, **47**, 558–561.

2 G. Kresse and J. Furthmüller, *Comput. Mater. Sci.*, 1996, **6**, 15–50.

3 J. P. Perdew, K. Burke and M. Ernzerhof, *Phys. Rev. Lett.*, 1996, **77**, 3865–3868.

4 J. P. Perdew and Y. Wang, *Phys. Rev. B*, 1992, **45**, 13244–13249.

5 P. E. Blöchl, *Phys. Rev. B*, 1994, **50**, 17953–17979.

6 S. Grimme, J. Antony, S. Ehrlich and H. Krieg, *J. Chem. Phys.*, 2010, **132**, 154104.

7 S. Grimme, S. Ehrlich and L. Goerigk, *J. Comput. Chem.*, 2011, **32**, 1456–1465.

8 J. Ruan, Y. Chen, G. Zhao, P. Li, B. Zhang, Y. Jiang, T. Ma, H. Pan, S. X. Dou and W. Sun, *Small*, 2022, **18**, 2107067.

9 L. Si, H. Li, Y. Zhang, D. Zhang, X. An, M. Yao, Y. Shao, J. Zhu and S. Hu, *Nano Res.*, 2023, **16**, 9116–9124.

10 W. Liang, Y. Wang, L. Zhao, W. Guo, D. Li, W. Qin, H. Wu, Y. Sun and L. Jiang, *Adv. Mater.*, 2021, **33**, 2100713.

11 F. Yang, J. Ye, L. Gao, J. Yu, Z. Yang, Y. Lu, C. Ma, Y.-J. Zeng and H. Huang, *Adv. Energy Mater.*, 2023, **13**, 2301408.

12 Y. Qiu, J. Fan, J. Wu, W. Lu, S. Wang, D. Wang, X. Ge, X. Zhao, W. Zhang, W. Zheng and X. Cui, *Nano Lett.*, 2023, 23, 9555-9562.

13 Y. Liu, C. Liu, Z. Chen, X. Zheng, R. Jiang, X. Tong, Y. Deng and W. Hu, *J. Mater. Sci. Technol.*, 2022, **122**, 148–155.

14 S. Han, Y. Ma, Q. Yun, A. Wang, Q. Zhu, H. Zhang, C. He, J. Xia, X. Meng, L. Gao, W. Cao and Q. Lu, *Adv. Funct. Mater.*, 2022, **32**, 2208760.

15 N. Ye, P. Zhao, X. Qi, R. Zhang, B. Yan, W. Sheng, Z. Jiang and T. Fang, *Appl. Catal. B,* 2023, **322**, 122142.

16 H. Xu, K. Wang, G. He and H. Chen, *J. Mater. Chem. A*, 2023, **11**, 17609–17615.

17 J. Wu, X. Cui, J. Fan, J. Zhao, Q. Zhang, G. Jia, Q. Wu, D. Zhang, C. Hou, S. Xu, D. Jiao, L. Gu, D. J. Singh and W. Zheng, *ACS Energy Lett.*, 2021, **6**, 1912–1919.

18 F. Gao, Y. Zhang, B. Zou, F. Jiang, Z. Li and Y. Du, *J. Colloid Interface Sci.*, 2022, **610**, 271–279.

19 B. Qiao, T. Yang, S. Shi, N. Jia, Y. Chen, X. Chen, Z. An and P. Chen, *Small*, 2021, **17**, 2006534.

20 F. Gao, Y. Zhang, P. Song, J. Wang, C. Wang, J. Guo and Y. Du, *J. Power Sources*, 2019, **418**, 186–192.

21 H. Kivrak and N. Aktas, *Int. J. Hydrog. Energy*, 2022, **47**, 35265–35274.

22 Z. Dong, X. Jiang, W. Zhang, J. Wang, G.-R. Xu, Z. Wu, G. Li and L. Wang, *J. Colloid Interface Sci.*, 2022, **623**, 1122–1131.

23 R.-L. Zhang, J.-J. Duan, Z. Han, J.-J. Feng, H. Huang, Q.-L. Zhang and A.-J. Wang, *Appl. Surf. Sci.*, 2020, **506**, 144791.

24 K. Dong, H. Pu, T. Zhang, H. Dai, X. Zhao, L. Zhou, K. Wang, Y. Wang and Y. Deng, *J. Alloys Compd.*, 2022, **905**, 164231.

25 D. P. Chen, X. C. Liu, X. D. Liu, L. Yuan, M. L. Zhong and C. Y. Wang, *Int. J. Hydrog. Energy*, 2021, **46**, 30455–30466.

26 F. Gao, Y. Zhang, P. Song, J. Wang, T. Song, C. Wang, L. Song, Y. Shiraishi and Y. Du, *J. Mater. Chem. A*, 2019, **7**, 7891–7896.

27 X. Zhou, Y. Ma, Y. Ge, S. Zhu, Y. Cui, B. Chen, L. Liao, Q. Yun, Z. He, H. Long, L. Li, B. Huang, Q. Luo, L. Zhai, X. Wang, L. Bai, G. Wang, Z. Guan, Y. Chen, C.-S. Lee, J. Wang, C. Ling, M. Shao, Z. Fan and H. Zhang, *J. Am. Chem. Soc.*, 2022, **144**, 547–555.

28 A. Cassani, N. Tuleushova, Q. Wang, H. Guesmi, V. Bonniol, J. Cambedouzou, S. Tingry, M. Bechelany, D. Cornu and Y. Holade, *ACS Appl. Energy Mater.*, 2021, **4**, 9944–9960.

29 H. Shang, H. Xu, C. Wang, L. Jin, C. Chen, G. Zhou, Y. Wang and Y. Du, *Nanoscale*, 2020, **12**, 3411–3417.

30 H. Du, K. Wang, P. Tsiakaras and P. K. Shen, *Appl. Catal. B Environ.*, 2019, **258**, 117951.

31 F. Gao, Y. Zhang, P. Song, J. Wang, B. Yan, Q. Sun, L. Li, X. Zhu and Y. Du, *Nanoscale*, 2019, **11**, 4831–4836.

32 D. Wang, Y. Zhang, Z. Li, Z. Wu, S. Hata, F. Gao, Y. Shiraishi and Y. Du, *J. Colloid*

Interface Sci., 2023, **636**, 602–609.

33 Z. Li, Y. Zhang, B. Zou, Z. Wu, F. Gao and Y. Du, *Inorg. Chem.*, 2022, **61**, 9693–9701.

34 J. Wang, W. Zhang, Z. Dong, N. Zhang, Q. Zhang, C. Xie, Z. Wu, G.-R. Xu and L. Wang, *Int. J. Hydrog. Energy*, 2022, **47**, 33319–33328.

35 Y. Zhang, F. Gao, P. Song, J. Wang, T. Song, C. Wang, C. Chen, L. Jin, L. Li, X. Zhu and Y. Du, *J. Power Sources*, 2019, **425**, 179–185.

36 Y. Zhang, J. Li, C. Wang, D. Liu, R. Yu, C. Ye and Y. Du, *J. Colloid Interface Sci.*, 2023, **647**, 519–527.